SIAM J. APPLIED DYNAMICAL SYSTEMS
Vol. 4, No. 1, pp. 159–186

Blinking Rolls: Chaotic Advection in a Three-Dimensional Flow with an Invariant*

P. Mullowney†, K. Julien†, and J. D. Meiss†

Abstract. We study a simple, nonautonomous, three-dimensional, incompressible flow corresponding to sequentially active two-dimensional rolls with distinct axes. A feature of the model is that an analytical map is obtained. We show that when the roll axes are orthogonal, motion is confined to two-dimensional topological spheres. The dynamics on each surface ranges from nearly regular to largely chaotic. We study the transport and mixing on each surface and their dependence upon parameters in the system.

Key words. chaotic advection, transport, mixing, volume-preserving mappings

AMS subject classifications. 76F25, 37B55, 70K55, 37D45

DOI. 10.1137/040606727

1. Introduction.

Eulerian velocity fields. Although the ABC flow is probably not physically observable, the crucial idea is that mixing can occur even in the simplest of flows in three dimensions [36]. In the two-dimensional case, transport can also be achieved in laminar, time-dependent flows. One of the seminal models was developed by Aref, who coined the term "chaotic advection" [1]. His flow, called the "blinking vortex," is specifically designed to yield nonintegrable Lagrangian trajectories. This model can be interpreted as an idealized mixing protocol where passive tracers are successively captured by the velocity fields of vortical stirrers that are the analogues of turbulent eddies with finite lifetimes.

In sections 2 and 3, we generalize the blinking vortex model and construct a physically motivated, yet mathematically simple, system with three-dimensional mixing. Our model, which we call "blinking rolls," replaces Aref's alternatively active vortices with alternatively active arrays of rolls aligned in di erent directions.

Though our mixing protocol is idealized, there is experimental evidence for the existence of similar flows. One such example is observed in Rayleigh–Bénard convection experiments for a binary mixture in a square cell with insulating sides. When the vertical temperature di erence exceeds a threshold value, an instability leads to a sequence of temporally alternating, orthogonal convection rolls whose axes are parallel to the square boundaries [34]. It is observed that "the transition from one set of rolls to the other is very fast, followed by a relatively long period of domination by one of the rolls ... the system lies most of the time in the roll patterns." Another example of roll-switching is the Küppers–Lortz instability for rotating convection in a pure fluid [28, 9, 43, 22, 42]. Rotation causes an instability that results in switching of the roll axes by roughly 60°. Theoretical and experimental studies have shown that the rolls switch with a characteristic frequency proportional to the relative temperature di erence above threshold.

When the switching occurs much faster than the roll turnover time, it can be idealized as instantaneous. In this case, the flow can be viewed as a composition of maps corresponding to the action of each individual roll. For the incompressible case, this gives a composition of volume-preserving maps. Transport in volume-preserving maps was studied in pioneering work on a discretized ABC system [37, 15, 12, 11]. The onset of transport is closely related to the destruction of heteroclinic connections for codimension-one manifolds [38, 29]; a Melnikov method was developed to study the bifurcations in manifold crossings in [30, 31].

It is generally di cult to find models for three-dimensional flows that both are mathematically accessible and have e ective transport. However, there is a small but growing link between mixing in experimental, three-dimensional flows and theoretical modeling based on chaotic advection. Shinbrot and his collaborators have studied the transient behavior of weakly buoyant tracers in a laminar flow within a cylindrical batch stirring device using a traveling wave map with a buoyancy term [40

model. In section 2 the flow for a single roll is constructed and the equations of motion are solved to obtain an analytical time-t map. In section 3 the flow with roll-switching is modeled by composing several of these maps. For the case that the roll axes are orthogonal, there is an invariant that constrains the motion to two-dimensional surfaces. In fact, we show in section 4 that the invariant persists regardless of the choice of stirring protocol. This system has a number of symmetries that simplify its analysis; see section 5. In section 6, we use normal form expansions to understand behavior near a fixed point and near roll boundaries. Numerical results are given in section 7.

2. Blinking rolls. Aref's blinking vortex flow corresponds to a two-dimensional, inviscid, incompressible fluid in a circular domain of radius a [1]. A point vortex moves inside the bounding contour according to a stirring protocol $(x(t), y(t))$. The equations for a passive scalar in such a fluid are Hamiltonian, and if the vortex position is constant in either a fixed or a steadily rotating coordinate system, then the flow is integrable. Otherwise, the flow is typically nonintegrable.

The blinking vortex corresponds to a stirring protocol with period T. For the first half of the period, a vortex resides at $(b, 0)$, and for the remainder of the period a vortex resides at $(-b, 0)$ for some $b < a$. For simplicity it is assumed that there is an instantaneous transition between the flows associated with the finite-lifetime point vortices. This allows the equations of motion for each half period to be solved exactly, giving rise to the half period maps $F_1(x, y)$ and $F(x, y)$. The Lagrangian tracer dynamics is then governed by the full period map $f = F \circ F_1$.

Two-dimensional transport can then be studied simply by iterating the map. The dynamics are governed by two dimensionless parameters $\mu = \frac{\Gamma T}{a^2}$, representing the vortex strength, and $\beta = \frac{b}{a}$

dependence, giving the general velocity field

$$\mathbf{v}(\mathbf{x}, t) = A(t) \quad \psi_1 \times \hat{\mathbf{e}}_1 + B(t) \quad \psi \quad \times \hat{\mathbf{e}}$$

functions [10] to obtain the flow

$$\Phi_t \begin{bmatrix} x \\ y \\ z \end{bmatrix} = \begin{bmatrix} x \\ \sin^{-1}(k\,\mathrm{sn}(At - M(y,z),k)) \\ \sin^{-1}(k\,\mathrm{sn}(At + N(y,z),k)) \end{bmatrix}$$

4. Existence of an invariant. Our numerical investigations for blinking orthogonal roll arrays indicate that three-dimensional mixing does not occur (see section 7). Indeed, these investigations led to the discovery that the flow has an invariant for this case. This was unexpected since invariants are not common for volume-preserving flows and mappings that have no apparent symmetries (though some special examples have been constructed in [20]). As we see here, the flow of (4) does have a symmetry, although it is not immediately obvious.

Indeed, there is an invariant for the case of three rolls if we choose the stream functions to have the separable forms

$$\psi_1 = g(y)h(z), \quad \psi = f(x)h(z), \quad \psi = f(x)g(y). \tag{10}$$

In this case it is easy to see that for *arbitrary* amplitude functions $A(t)$, $B(t)$, and $C(t)$ (i.e., *arbitrary* stirring protocol), the function

$$J = f(x)g(y)h(z) \tag{11}$$

is an invariant for the flow. To see this in a pedestrian way, one need only show that

$$\frac{dJ}{dt} = J(\mathbf{x}) \cdot \mathbf{v}(\mathbf{x}, t) = 0, \tag{12}$$

as is easy to demonstrate using (4).

More generally, if $J = 0$, then (12) implies that there exists a vector field

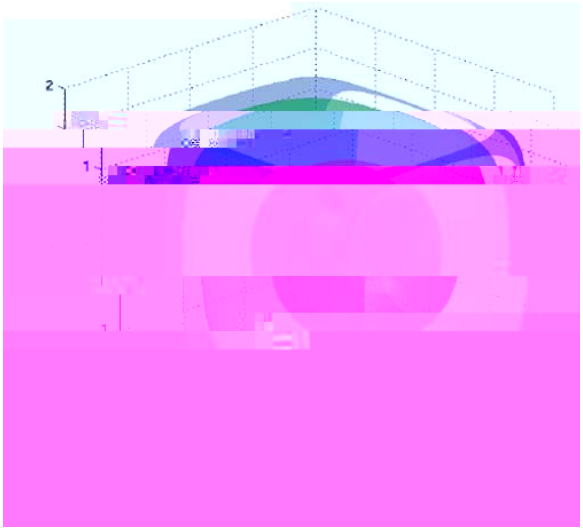

Figure 3. *Three level sets of the invariant* (14). *The gaps in the outer surface are used to illustrate the concentric structure of the level sets.*

5. Symmetries. The trigonometric roll (3) is periodic with period 2π and is odd under translation by π in y or z. This implies that the fundamental cube for the three-dimensional flow (4) is divided into eight cells with alternating rotation directions; the case that all $T_i > 0$ is shown in Figure 4. The ± signs in the figure indicate the directions of right- (left-) handed

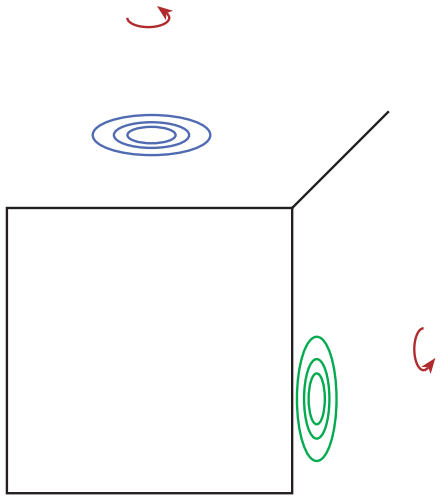

and all cyclic permutations. Similarly, for the reflection,

$$H_1 \circ F \circ H_1 = F^{-1}, \qquad H_1 \circ F \circ H_1 = F^{-1},$$

and all cyclic permutations. Using these, we obtain

$$H_k \circ F_i \circ F_j \circ H_k = \begin{cases} F_i^{-1} \circ F_j & \text{if } k = j = i, \\ F_i \circ F_j^{-1} & \text{if } k = i = j, \\ F_i^{-1} \circ F_j^{-1} & \text{if } k = i \text{ and } k = j. \end{cases} \tag{17}$$

From this we conclude that once a particular i and j are picked, the direction of rotation for each component is irrelevant because the maps are all conjugate to one another.

We next show that maps with di erent choices of i and j are conjugate. As the axes can be mapped onto each other by rotations, we consider

$$S_k^{-1} \circ F_i(T_i) \circ F_j(T_j) \circ S_k \quad \text{for } i = j,$$

which switches one or both axes of rotation depending upon the choice of k. Here we have explicitly put in the parameter T, since it will be important below. First, for the case $k = i$,

$$S_i^{-1} \circ F_i(T_i) \circ F_j(T_j) \circ S_i = \begin{cases} F_i(T_i) \circ F_{i-}(T_j) & \text{if } j = i - 1, \\ F_i(T_i) \circ F_{i+}^{-1}(T_j) & \text{if } j = i + 1, \end{cases}$$

where the indices are understood modulus 3. Next, if $k = j$, then

$$S_j^{-1} \circ F_i(T_i) \circ F_j(T_j) \circ S_j = \begin{cases} F_{j-}(T_i) \circ F_j(T_j) & \text{if } i = j - 1, \\ F_{j+}^{-1}(T_i) \circ F_j(T_j) & \text{if } i = j + 1. \end{cases}$$

Combining these relations with (17) shows that maps with all possible choices of di erent axes and di erent rotation directions are conjugate to one another. The critical point is that the first roll must be active for time T_j, and the second roll must be active for T_i as stated originally in (16).

Finally, for the case when $k = j = i$, we find

$$\begin{aligned} S_k^{-1} \circ F_i(T_i) \circ F_j(T_j) \circ S_k &= \begin{cases} F_j^{-1}(T_i) \circ F_i(T_j) & \text{if } k = j + 1, \\ F_j(T_i) \circ F_i^{-1}(T_j) & \text{if } k = j - 1 \end{cases} \\ &= F_j^{-1}(T_i) \circ F_i^{-1}(T_j) \quad \text{by (17)} \\ &= (F_i(T_j) \circ F_j(T_i))^{-1} \end{aligned}$$

i9573 154607781 356.5264 207.2368 Tm ()))Tj /F2 1 T15203385 1.388342

Thus

We denote the map in the new coordinates $\mathbf{u} = (u, \bar{u}, w)$ by F, so that $DF(0) = \Lambda$. Expand F in a power series expansion of the form

$$F(\mathbf{u}) = \Lambda(\mathbf{u} + F^{(k)}(\mathbf{u}) + F^{(k+1)}(\mathbf{u}) + \cdots),$$

where $F^{(k)}$ is a term that is homogeneous of degree $k > 1$ in the variables $\mathbf{u}$, i.e.,

$$F^{(k)} = \sum_{m+n+p \quad k} a_{m,n,p} u^m \bar{u}^n w^p , \tag{18}$$

with $m, n, p \in \mathbb{Z}_+$, and complex coefficients $a_{m,n,p}$. Since the original map is real, $\bar{u}$ is the complex conjugate of u, and thus $\bar{a}_{m,n,p} = a_{n,m.p}$.

The normal form for F is a "simpler" map G that is conjugate to F,

$$G(h(\mathbf{u})) = h(F(\mathbf{u})), \tag{19}$$

by a near identity transformation h. As usual we expand the conjugacy h and the new map in power series and at each order use h to remove as many terms in G as possible. At order

As demonstrated in section 5, the map (6) has reflection symmetry through the origin. In this case, the normal form will exhibit the same symmetry, and therefore all even order terms drop out of the expansion so that

$$\alpha_{n,\,p+1} = \beta_{n,\,p+1} = 0.$$

In addition, if F is volume-preserving, then we can choose h so that it also preserves volume, and therefore the normal form will as well:

$$du'\ \ d\bar{u}'\ \ dw' = du\ \ d\bar{u}\ \ dw.$$

This places restrictions on the coe cients of (21). To cubic order, we find

$$\beta_{,0} = -4\mathrm{Re}(\alpha_{,0}), \qquad \beta_{0,} = -\frac{2}{3}\mathrm{Re}(\alpha_{0,}). \tag{22}$$

Now, we can analyze basic phenomena of the normal form. Letting $u = \rho e^{i}$, we can rewrite (21) to obtain the real map

$$\begin{aligned}
\rho' &= \rho\left(1 - \frac{1}{4}\beta_{,0}\rho - \frac{3}{2}\beta_{0,}w + O(3)\right),\\
\theta' &= \theta + \omega + \mathrm{Im}(\alpha_{,0})\rho + \mathrm{Im}(\alpha_{0,})w + O(3),\\
w' &= w(1 + \beta_{,0}\rho + \beta_{0,}w + O(3)).
\end{aligned}$$

Thus the origin is a nonhyperbolic fixed point. To all orders, the w-axis ($\rho = 0$) and the equatorial plane $w = 0$ are invariant. The plane $w = 0$ is locally an (un)stable manifold of the origin when $\beta_{,0} > 0$ (< 0), and the w-axis is locally (un)stable when $\beta_{0,} < 0$ (> 0). There are additional unstable manifolds along the lines $\rho = sw$ when $s = -2\frac{\beta_{0,2}}{\beta_{2,0}} > 0$, and these are (un)stable manifolds when $\beta_{0,} > 0 (< 0)$. An example is shown in Figure 5.

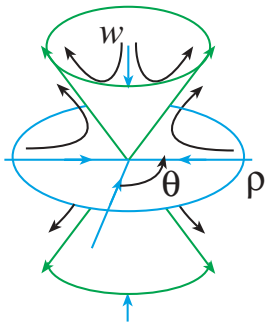

Figure 5. *Dynamics of the normal form in the* $(\ ,\ )$*-plane for* $_{2,0} > 0$ *and* $_{0,2} < 0$.

Note that when there is an invariant whose surfaces are topological spheres about the origin (as is the case for (6)), none of the invariant axes can be attracting or repelling. Thus the only normal form that corresponds to this case is one in which *every* resonant coe cient has real part zero. Thus the normal form for (6) with irrational ω fixes ρ and w, and every orbit near the origin lies on an invariant circle. As we will see, this corresponds well with the numerical observations of the dynamics of (6) in section 7.

6.2. Motion on the boundary cube. The single roll flow (9) preserves the boundaries of the fundamental cube; the surfaces where x, y, or z are $\pm -$. Recall from section 2 that the line $(y, z) = (-, -)$ and its translations by $(m\pi, n\pi)$ consist of saddle equilibria of Φ_T. The four faces corresponding to the set $\{(y, z) : |y| = - \text{ or } |z| = -\}$ correspond to their stable and unstable manifolds.

On these faces, the velocity field (3) has only one component, and its flow simplifies since there the modulus $k \to 1$, and $\mathrm{sn}(T, 1) = \tanh(T)$, and $\mathrm{cn}(T, 1) = \mathrm{dn}(T, 1) = \mathrm{sech}(T)$. In this case (9) becomes

$$\Phi_T(x, y, z) = \begin{cases} \left(x, y, \sin^{-1}\left[\dfrac{\mathrm{s}\,(T)\,\mathrm{si}\,(z) \pm \mathrm{si}\,(T)}{\mathrm{s}\,(T) \pm \mathrm{si}\,(z)\,\mathrm{si}\,(T)}\right]\right) & \text{if } y = \pm -, \\ \left(x, \sin^{-1}\left[\dfrac{\mathrm{s}\,(T)\,\mathrm{si}\,(y) \mp \mathrm{si}\,(T)}{\mathrm{s}\,(T) \mp \mathrm{si}\,(y)\,\mathrm{si}\,(T)}\right], z\right) & \text{if } z = \pm -. \end{cases} \tag{23}$$

This formula for $T = T_1$ gives the boundary map corresponding to F_1; we denote it as B_1. The maps B and B are obtained from (23) by permuting the variables appropriately.

It is convenient to use a spherical projection to display the dynamics of the system. Letting (θ, η) denote the longitude and colatitude, respectively, we can project the cube onto the sphere. Then the dynamics can be displayed on the rectangle $-\pi < \theta \le \pi$, $0 \le \eta \le \pi$. For example, in Figure 6 we show F_1 and F in this projection. In this figure, the twelve edges of the cube project to the red curves. The faces $x = \pm -$ are pierced in the center by the points $(\theta, \eta) = (0, -)$ and $(\theta, \eta) = (\pi, -)$, respectively. The faces defined by $z = \pm -$ correspond to

intersections of the red curves in Figure 6. The edges of the cube now comprise parts of the

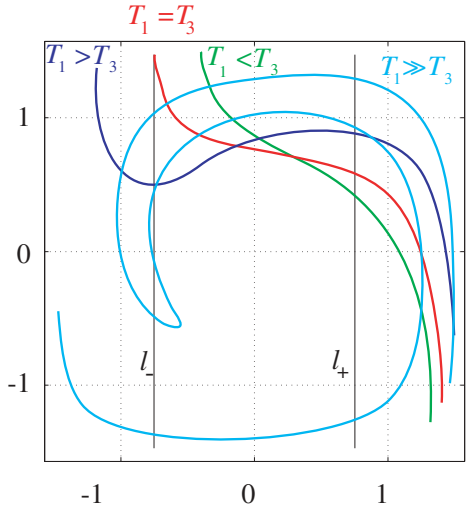

Figure 7. *Fixed points of* $\sqrt{\Pi} \circ B_3$ *at* $= \frac{\pi}{2}$. *Here* $\boldsymbol{l}_+ = B_3(\boldsymbol{l}_-)$ *and the colored curves are images of* $\boldsymbol{l}_+$ *under* $\sqrt{\Pi}$.

7. Numerical explorations. In this section we will explore some of the dynamics (6). For simplicity, we set $T = 0$ so that the second roll is not active, giving the system

$$F = F_1 \circ F . \tag{25}$$

As we showed in section 5, it is su cient to consider to $T_1 > T > 0$.

First we discuss the techniques that we will use to visualize the orbits of (25). We take advantage of the fact that orbits are constrained to surfaces of constant $J(x, y, z) = \cos(x)\cos(y)\cos(z)$, and that for each $0 < J \leq 1$ these surfaces are convex, topological spheres; recall Figure 3. Therefore, as we did in section 6.2 for the maps on the boundary, we can use spherical coordinates to obtain a two-dimensional projection of the dynamics. Letting (θ, η) be the spherical angles, any point (x, y, z) corresponds to a point (J, θ, η), and since J is invariant, we can view the dynamics in the angle plane. The coordinate transformation is thus

$$(J, \theta, \eta) = V(x, y, z) = \left(\cos(x)\cos(y)\cos(z), \tan^{-1}\left(\frac{y}{x}\right), \tan^{-1}\left(\frac{\sqrt{x^2 + y^2}}{z}\right) \right), \tag{26}$$

which has the Jacobian

$$\det(DV) = J \frac{x \tan x + y \tan y + z \tan z}{\sqrt{x^2 + y^2}\,(x^2 + y^2 + z^2)} . \tag{27}$$

To visualize the dynamics on the (θ, η)-plane for a given invariant value, we will iterate a grid of initial conditions. For each (θ, η), we first determine the radius, r, using the Newton method on $J(r \sin\eta \cos\theta, r \sin\eta \sin\theta, r$

radius and plot (θ, η) along the orbit. To view the dynamics in the entire cube, we choose a grid in J (from 1 to 0) and concatenate the figures to create the animations 60672_01.avi and 60672_02.avi. The animations reveal a system rich in complex, chaotic behavior.

Recall that when a map has an invariant, fixed points generically come in one-parameter families labeled by the invariant value [20]. Suppose that $O = \{x_t, t = 0, \ldots, n-1\}$ is a periodic orbit of period n. Di erentiating the equation $J(F^n(x)) = J(x)$ at the point x_0 gives

$$(DF^n(x_0))^T \cdot \quad J(x_0) = \quad J(x_0). \tag{28}$$

Thus when $J(x_0) = 0$ (as is true on all invariant surfaces except the origin and the fundamental cube), this vector is a left eigenvector of the Jacobian with unit multiplier. Since F is volume-preserving, this implies that the multipliers of O are $(1, \lambda, \frac{1}{\lambda})$. When $\lambda = 1$, the implicit function theorem can be used to show there is a curve of fixed points of F^n parameterized by J through x_0. When $\lambda = \pm 1$, the periodic orbit is elliptic on the invariant surface if λ is on the unit circle and hyperbolic when λ is real. The orbit generically undergoes q-tupling bifurcations when λ passes through the value $e^{i\omega}$ with $\omega = p/q$ rational. These bifurcations correspond to the creation of new periodic orbits of period nq; these new orbits are also found in one-parameter families parameterized by J.

To compute some of the low period orbits we use Broyden's method [16]. For the fixed points, we allowed the initial guess for Broyden's method to range over the entire invariant surface, so that we had a good chance of finding all of them. However, to limit the complexity of the figures, we decided only to search for periodic points born at the q-tupling bifurcations of the fixed points. An analytic expression for the Jacobian can be computed to determine the stability of the periodic points.

The analysis of fixed and periodic points gives us the ability to understand the fine structure of the system. It also illuminates any barriers to global transport on each invariant. For instance, the existence of large islands surrounding stable periodic points inhibits the transport of passive scalars. On the other hand, the existence of hyperbolic periodic points should aid transport due to the likelihood of homoclinic and heteroclinic tangles in their manifolds.

One measure of the degree of chaos in a system are its Lyapunov exponents. Since F is volume-preserving, the sum of its three exponents must be zero, and because the orbits are restricted to two-dimensional surfaces, one of the exponents must be exactly equal to zero. This implies that the remaining two exponents are equal in magnitude and opposite in sign. We use the iterative QR method to compute the exponents [21]. Along an orbit O, define

$$Q^{(n+1)} R^{(n+1)} = DF(x_n) Q^{(n)} R^{(n)},$$

where $Q^{(0)} = R^{(0)} = id$. As usual Q is orthogonal and R is upper triangular. To compute the exponents, we require that $R_{ii} > 0$; it is not hard to show that one can modify the QR method so that this is the case. Moreover, since F is orientation-preserving and $\det(R) > 0$, then $Q \quad SO(3)$. Thus we can represent Q with three angles, θ_i (for example, Euler angles or rotations about three orthogonal axes). Since

$$R^{(n+1)} (R^{(n)})^{-1} = (Q^{(n+1)})^T DF(x_n) Q^{(n)}$$

is upper triangular, this requirement can be manipulated to provide a formula for updating the angles θ_i iteratively. After n steps, the ith Lyapunov exponent is approximately

$$\lambda_i^{(n)}$$

of the orbits lie on invariant circles, as suggested by the normal form analysis in section 6.1. The apparent change in topology of the circles in the figure is due only to nonalignment of the spherical projection with the rotation axis. Note that the reflection symmetry through the origin implies that the northern and southern hemispheres have conjugate dynamics.

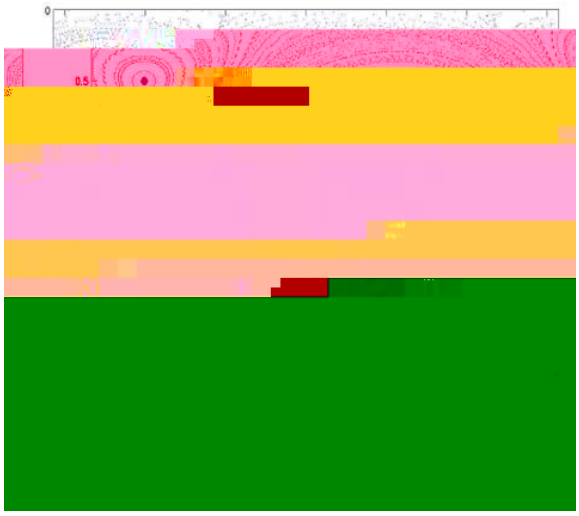

Figure 8. *Projection of the dynamics of* (25) *onto the* (,)*-plane for* $_1 = 7$, $_3 = 5$, *on the invariant surface* $= 0.973962$.

There is a curve of fixed points tangent to the v -axis at the origin; this gives rise to a pair of fixed points on each invariant surface, and for these parameter values there are no other fixed points. We focus on the fixed point in the northern hemisphere—by symmetry the other fixed point has the same behavior. In Figure 9, we plot the multipliers (1

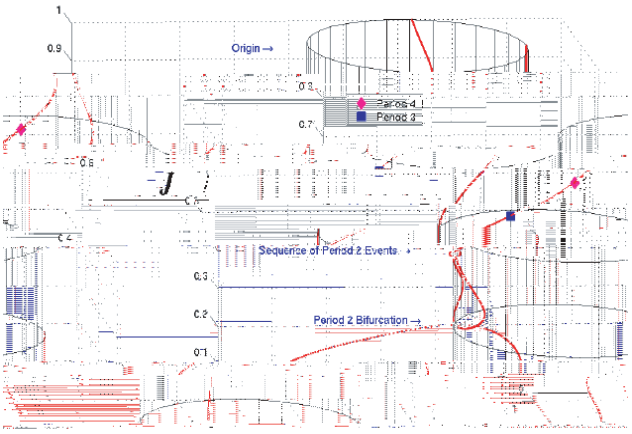

Figure 9. *Multipliers of the fixed point of* (25) *as a function of* J *for* $\alpha_1 = 7$ *and* $\alpha_3 = 5$. *Doubling, tripling, and quadrupling bifurcations are noted.*

thus spawning an unstable period-two orbit. At $J \approx .448222$, the unstable period-two orbit created from the previous split undergoes a pitchfork bifurcation, thus creating a pair of unstable period-two orbits and a stable period-two orbit. When the sequence finishes, we have a stable fixed point, two stable period-two orbits, and two unstable period-two orbits. There is a final supercritical doubling of the fixed point near $J = 0.27$, and for all smaller values of J, the fixed points are unstable.

In the QuickTime file 60672_01.avi, we present an animation of the dynamics and maximal Lyapunov exponent for these parameter values. The movie consists of 399 frames starting at $J = .999$ and decreasing to $J = 0$.

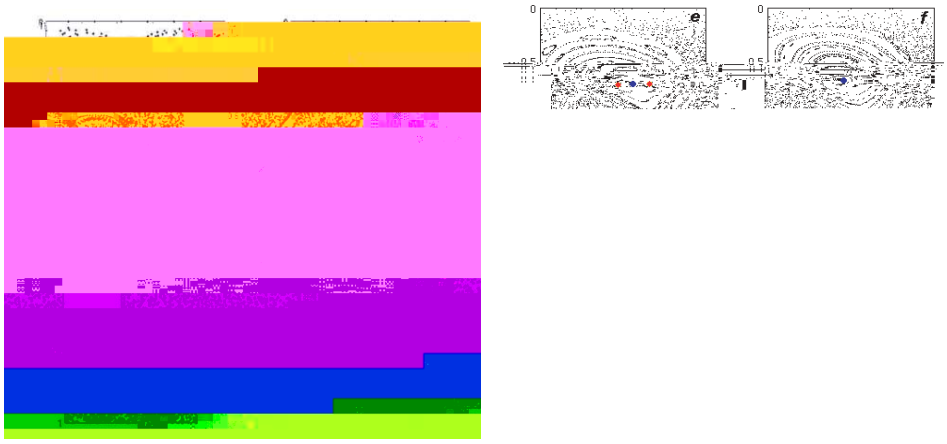

Figure 10. *Tripling and doubling bifurcations of a fixed point for* $_1 = 7$, $_3 = 5$. *The fixed point is shown as the blue circle, the green diamond and purple square correspond to stable and unstable period-three orbits, and the red diamond and yellow square are stable and unstable period-two orbits. The four panels at the left correspond to the following:* (a) $= 0.625940$, *just after the first subcritical pitchfork bifurcation. (For resolution in our figures, the full phase plane is not shown. Hence one stable period-three point is omitted. Two additional unstable period-three points are shown (bottom left, bottom right) which are part of another unstable period-three orbit.)* (b) $= 0.618429$, *just before tripling bifurcation.* (c) $= 0.600902$. (d) $= 0.578368$ *after the tripling. The right panels correspond to* (e) $= 0.465699$ *and* (f) $= 0.450677$, *just before and after the first supercritical doubling, and* (c) $= 0.445669$ *and* (d) $= 0.428143$, *after the second subcritical doubling and pitchfork bifurcations.*

Figure 11. *Phase plane and the Lyapunov exponent for* $= 0.262895$. *Points in the phase plane (upper panel) correspond to periodic orbits; colors are the same as in Figure*

of the phase portrait are indicated on the figure. The scaled average Lyapunov exponent remains nearly zero as J decreases from 1, until near $J = 0.8$, when $\frac{\langle\rangle}{T}$ suddenly begins to increase. This suggests that the asymptotic validity of the normal form breaks down near this point and corresponds with the appearance of small zones of chaotic behavior. At the quadrupling and tripling bifurcations, $\frac{\langle\rangle}{T}$ reaches local maxima, and two local minima are

almost immediately.

7.2. Example 2: $T_1 + T_3 = 6$. In this section we fix the total time to $T_1 + T = 6$, half of the previous value. We will first consider the case T_1

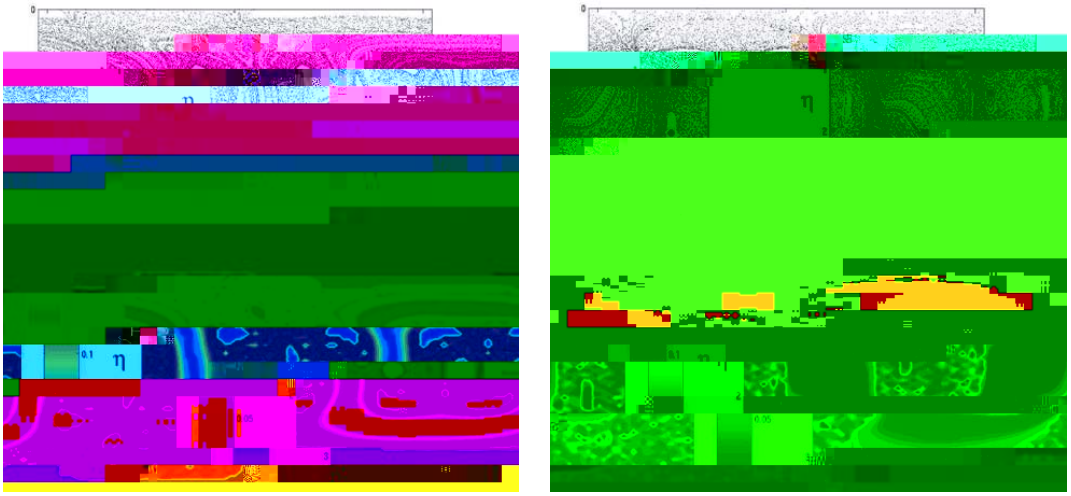

Figure 15. *Dynamics for* $_1 = 3.5$, $_3 = 2.5$. *The left panels correspond to* $= 0.282925$ *and the right to* $= 0.030045$. *Clicking on the above images displays the associated movie* (60672_02.avi).

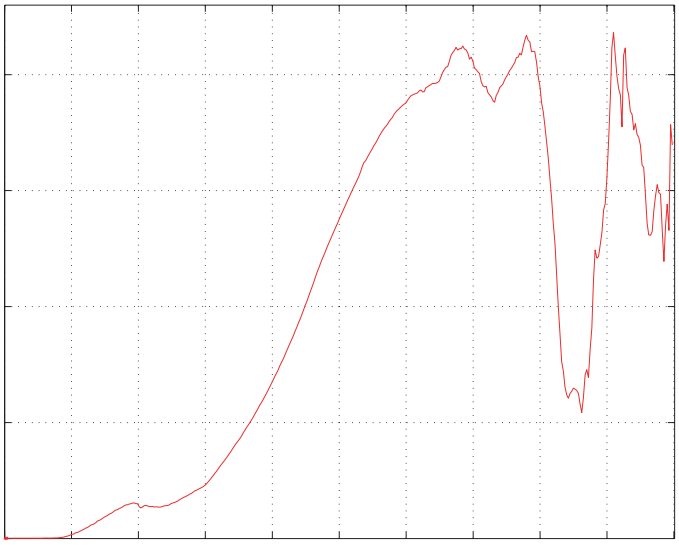

anomalous di usion theory [24, 27, 26, 25]. In a construction analogous to the Küppers–Lortz phenomenon, roll arrays rotating by 60° also display three-dimensional mixing. We will report on these topics in a future paper.

Acknowledgments.